ADVANCED FUNCTIONAL MATERIALS
www.afm-journal.de

Check for updates

An Electrical Switch-Driven Flexible Electromagnetic Absorber

*Hualiang Lv, Zhihong Yang, Hongbin Xu, Liuying Wang, and Renbing Wu**

The development of a thin, tunable, and high-performance flexible electromagnetic (EM) absorbing device that aims to solve signal interference or EM pollution is highly desirable but remains a great challenge. Herein, demonstrated is a flexible electrical-driven device constructed by an insulated organic-polymer substrate, carrier transmission layer, and core–shell structured absorber, enabling a narrow and tunable effective absorption region (f_E < 2.0 GHz) by controlling the external voltage toward this challenge. As a key design element, the selected absorber consists of an Sn/SnS/SnO_2 core and C shell, which exhibits an exceptional dielectric-response ability at a small voltage, which is attributed to desirable carrier mobility and excitable carriers. Multiple f_E-tuning regions (maximum up to 7.0), covering 90% of C-band can be achieved for Sn/SnS/SnO_2@C-based flexible device by selecting a low voltage (2–12 V). The strategy developed here may open a new avenue toward the design of flexible intelligent EM device for practical applications.

1. Introduction

The rapid development of wireless techniques, particularly fourth or fifth generation of network, wireless electronics, or artificial intelligence provides us a convenient and intelligent life.[1] Meanwhile, the electromagnetic (EM) pollution generated by these electronics is ever-increasingly than before. In particular, the working frequency of currently electronics are mainly ranging from S- and C-band (2.0–8.0 GHz), thus EM pollution from this region has become a serious concern.[2] Whereas, the available absorbing materials even with a desirable performance are hard to satisfy such requirement.[3–5] Taking Co/C as an example, it exhibits a good absorption in higher frequency region (12.9–18.0 GHz) but not in our wanted region (2.0–8.0 GHz).[6] If tuning effective absorption (f_E) toward lower frequency range, a larger absorption layer thickness (d) is required according to a quarter wavelength theory.[7] Unfortunately, it may not be a good solution as the larger coating thickness may result in the increase in both the cost and weight. Currently, the critical requirement on the d of the absorber should be less than 2.0 mm.[8] Therefore, tuning f_E toward lower frequency region is still a significant challenge for conventional EM absorbers.[9–11] In addition to matched region, an advanced absorbers should be intelligent, enabling a tunable of f_E in 2.0–8.0 GHz. Furthermore, compared with broad absorption, a narrow absorption may be more suitable for a specific device, in case to ensure a highly qualify signal transmission for others. In this regards, f_E is requested to be a narrow and tunable under a fixed thickness, which has never been reported.

On the other hand, recent studies showed that a desirable performance may be realized by the synergistic effect of external stimulation and absorbers.[12–14] In particular, electrical driven is an efficient and easy-controllable route to tune the absorption performance if selected material exhibits an excellent electrical tunable (ET) performance.[15] Once applying a voltage, the intrinsic dielectric can be altered, which in turn influence EM performance.[16] Both relative complex dielectric (ε_r) and dielectric loss (ε'') determine f_E region and intensity (estimated by reflection loss, RL).[17] Commonly, only the frequency region with RL < −10 dB (qualified value, representing 90% of absorption) can be denoted as an effective absorption region.[18] Hence, a qualified f_E is actually dependent on the matched ε_r and ε'' pairs (ε_r–ε''), if d is a constant.[19,20] Due to the close correlation between permittivity and voltage, it may open a new avenue toward the design of intelligent absorber by selecting a suitable ET material within a small voltage. Accordingly, a desirable ET performance is required to be a strong dielectric response ability within a small voltage.

Herein, a novel core–shell composite consisting of metal/oxide hybrid core encapsulated by amorphous carbon shell was developed and investigated as an ET absorber. Within this composite, the phase and composition of the hybrid core can be linearly tuned through a tailored carbonization process. Specifically, the metal Sn can be generated by the reduction of SnO_2 in the presence of the carbon shell during the heat treatment and the reduction degree is highly associated with the carbonization

Dr. H. Lv, H. Xu, Prof. R. Wu
Department of Materials Science
Fudan University
Shanghai 200433, P. R. China
E-mail: rbwu@fudan.edu.cn

Prof. Z. Yang
College of Material Science and Technology
Nanjing University of Aeronautics and Astronautics
Nanjing 210016, P. R. China

Prof. L. Wang
Xi'an Research Institute of High Technology
Xi'an 710025, P. R. China

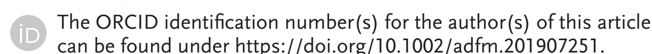
The ORCID identification number(s) for the author(s) of this article can be found under https://doi.org/10.1002/adfm.201907251.

DOI: 10.1002/adfm.201907251

 © 2019 WILEY-VCH Verlag GmbH & Co. KGaA, Weinheim

temperature. As expected, at elevated voltages, a qualified ε_r–ε'' pairs with $f_E < 2.0$ GHz ranging from 2.0 to 8.0 GHz could be achieved in this ET-driven composites according to ET calculation and EM simulation results. Inspired by the excellent ET performance as well as the ET simulations, we further designed a flexible intelligent EM absorbing device using parylene-c, core–shell composites (Sn/SnS/SnO_2@C) and multi-walled carbon nanotubes (MWCNTs) as an insulated substrate, an absorber, and a carrier transmission layer, respectively. The f_E region of as-designed device with operation voltage ≤18 V could be tuned in almost cover 4.0–8.0 GHz band with a fixed d of 2.0 mm, and the corresponding tunable bands (N) was up to 7, representing a new level in flexible EM absorbing device.

2. Results and Discussions

The choice of an appropriate ET absorber is of great importance for EM absorbing device performance. Commonly, EM absorber primarily originates from magnetic and dielectric-based materials. As for magnetic absorbers (e.g., Fe_3O_4, $CoFe_2O_4$, Fe, Co, Ni and magnetic hybrids), permeability value cannot be regulated by external voltages (Figure S1, Supporting Information). Hence, growing attentions have been focused on dielectric materials due to the fact that only permittivity requires to be considered (permeability is a constant value of 1.0).[21] Consequently, the correlation between dielectric and EM performance can be easily revealed by EM simulation (based on ASTM Standard 893-1997). **Figure 1**a and Figure S2 (Supporting Information) show the results of qualified ε_r–ε'' pairs at given thickness of 1.0, 1.2, 1.4, 1.6, 1.8, and 2.0 mm, respectively (for commercial application, thickness should be less than 2.0 mm). Subsequently, the thickness dependent of effective coverage is listed in Figure 1b. It can be seen that the effective coverage of S-band (2.0–4.0 GHz) equals to zero under 1.0–2.0 mm. The maximum coverage for C-band (4.0–8.0 GHz) can reach 90% under a thickness of 2.0 mm. To maximize a tunable region, the thickness is fixed at 2.0 mm. On this basis, the qualified ε_r–ε'' pairs are further optimized with the requirement of $f_E < 2.0$ GHz. The result is presented in Figure 1c, from which the effective ε_r ranges in 20–60, and the corresponding ε'' mainly varies in 4–12 (partial value up to 18). Based on the EM simulation results, the initial permittivity of the selected ET material should be smaller than lower limit of desirable ε_r–ε'' pair for the tuning by voltage (note that permittivity only can be increased by external electrical field). After making a summarization of ε_r–ε'' (Figure 1d), one material that satisfies this requirement mainly concentrates on carbon-oxide/sulfide, carbon-metal-oxide/sulfide or semiconductor heterojunction. Limited by the conductivity, the significant improvement of permittivity can be observed at a relative high activated voltage (denote as V_a) for carbon-oxide/sulfide or semiconductor heterojunction. For example, we found that the V_a values of C/MnO_2 ($V_a = 12$ V), C/$NiCo_2S_4$ ($V_a = 14$ V), and g-C_3N_4/ZnO ($V_a = 16$ V) were larger than 10 V (Figure S3, Supporting Information), suggesting the poor ET performance. As compared to carbon-oxide/sulfide or semiconductor heterojunction, carbon-metal-oxide/sulfide composites may be a desirable candidate, owing to their improved conductivity. Due to the existence of metal, the initial permittivity can be enlarged. Therefore, each component of selected material can be fine-tuned to balance V_a and initial permittivity.

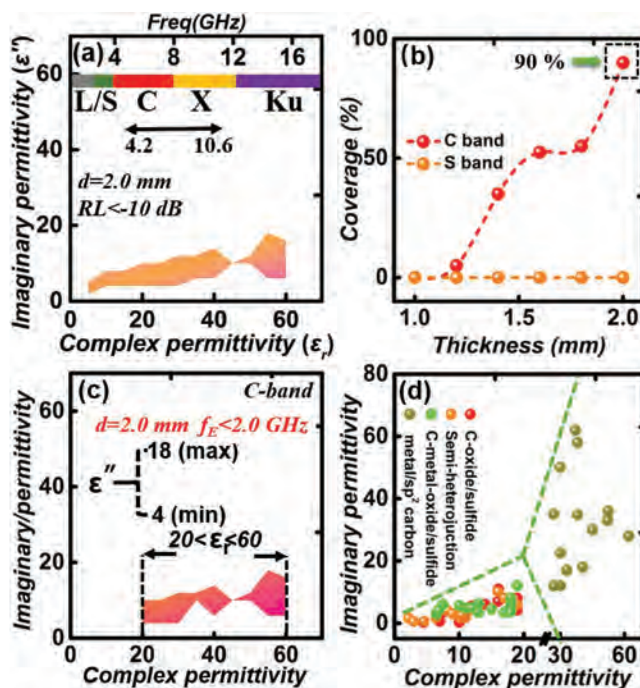

Figure 1. a) EM simulation results with a given thickness of 2.0 mm; b) the thickness dependent of C- and S-band coverage; c) the optimized ε_r–ε'' pairs with a $f_E < 2.0$ GHz (ranging in C-band, thickness = 2.0 mm); d) summarization of the ε_r–ε'' values of previously reported absorbers (different colors present the magnetic systems).

Combination with EM simulation, we first developed a core–shell structured composite with Sn/SnO_2 as the core and amorphous carbon as the shell to reveal the ET performance. The ratios of Sn, SnO_2, or C shell can be linearly tuned through a tailored carbonization temperature. **Figure 2**a shows the schematic illustration of phase conversion process from precursor to resulting products. SnO_2@polysaccharide biopolymer (denoted as SnO_2@PB) is generated at the initial stage by a hydrothermal route (Figure S4a, Supporting Information). The as-obtained SnO_2@PB sample (Sn-60, obtained by using 6 g glucose) presents an obviously core–shell structure. The average particle size of each sample is nearly 100 nm. Figure S4b (Supporting Information) shows the transmission electron microscopy (TEM) image of samples further treated at 600–750 °C, in which significant changes can be observed in respective core. To better understand the evolution of morphologies, the close views of cores obtained at temperatures of 600–750 °C are given in Figure 2b. At 600 °C, only carbonization occurs and thus no any changes are found in the morphology of the core. While for the samples annealed at 650 °C, SnO_2 is partially reduced to Sn, thus the size of core is reduced, due to the loss of O element. With further increasing of the annealing temperature, more and more SnO_2 could be reduced and the core becomes much looser. Upon the complete conversion from SnO_2 to Sn, the degree of loser can reach the maximum value in this stage, which looks like a "hollow" structure. All the phase conversion

© 2019 WILEY-VCH Verlag GmbH & Co. KGaA, Weinheim

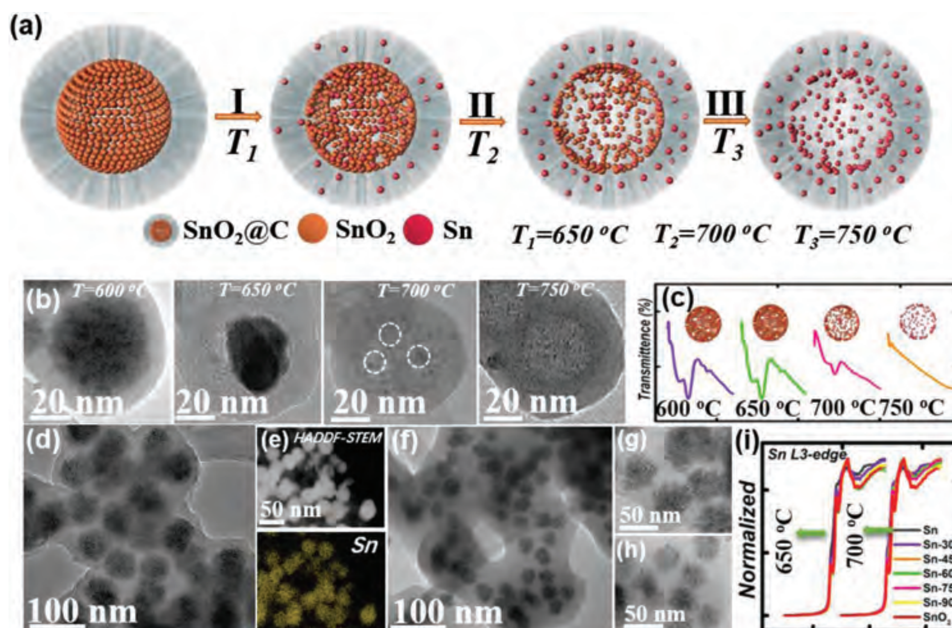

Figure 2. Phase, morphology, and structure characterizations. a) Schematic illustration of the formation process of Sn/SnO_2@C ternary hybrids; b) TEM images of core-evolution gained at temperature ranging from 600 to 750 °C (all samples obtained with the usage of 6 g glucose). c) FT-IR spectra of the SnO_2@PB treated at 600–750 °C; d) TEM image and e) HADDF-STEM image of flake-shaped SnO_2@PB (precursor) with multiple-cores (Sn-75, prepared with 7.5 g glucose); f) TEM images of flake-shaped SnO_2@PB (precursor, Sn-90); g,h) magnified TEM images of Sn-75 and Sn-90; i) Sn L3-edges of Sn/SnO_2@C samples obtained at 650 and 700 °C.

process can be confirmed by the X-ray diffraction (XRD) patterns and Fourier transform infrared (FT-IR) spectrum. In the XRD patterns (Figure S4c, Supporting Information), the SnO_2 characteristic peaks can be easily identified in all these samples treated at 600–700 °C. Additionally, the diffraction peaks of Sn appear at 650 °C and the relative peak intensities of Sn to SnO_2 become stronger with increasing the annealing temperature, indicating the improvement in the reduction degree. Due to the complete reduction, only Sn diffraction peaks can be observed at 750 °C. It should be noted that no any amorphous carbon can be detected in distinct diffraction peaks. The phase conversion procedure at various temperatures can be also reflected in the FT-IR spectra, as shown in Figure 2c. Excepting Sn@C, other samples have two peaks at 518 and 648 cm^{-1}, representing the vibration of Sn-O bonds. The peak intensities become weak with increasing the annealing temperatures, which is also in agreement with the XRD results. The mechanism for linearly tuning content of Sn at various temperatures may be attributed to the released reduction gas (e.g., CO and H_2) and carbon, as confirmed by Raman spectra and X-ray photoelectron spectrum (XPS) results (Figure S4d,e, Supporting Information).

In addition to the ratio of Sn/SnO_2, the total content of carbon can be tuned by adjusting the amounts of carbon precursor (refer to glucose). In the control experiments, the SnO_2@PB samples with various glucose adding amounts (3, 4.5, 7.5, and 9.0 g) are synthesized and the samples can be termed as Sn-30, Sn-45, Sn-75, and Sn-90, respectively. The structures of Sn-30 and Sn-45 show no significant difference, as compared to former Sn-60 (Figure S4f, Supporting Information). In Figure 2d,e, the SnO_2@PB (Sn-75) prepared with higher content of carbon precursor (7.5 g) are stacked together, leading to a multi-core flake structure according to TEM and high-angle annular dark-field scanning transmission electron microscopy (HADDF-STEM) observations. Continuing to 9.0 g, the carbon flake inserted by multi SnO_2 cores can be obtained, as confirmed by TEM and HADDF-STEM in Figure 2f. Close the image, the sizes of SnO_2 cores distinctly decrease with increasing of carbon precursor (Figure 2g,h). Through the Nano measurer software, the average sizes of cores are ≈39 and 26 nm for Sn-75 and Sn-90 products, respectively (Figure S4g, Supporting Information). The core sizes of SnO_2 decrease with the increase of the carbon precursor, possibly due to the fact the creation of more polysaccharide monomer from carbon precursor in the surrounding of SnO_2 nanocrystals can effectively prevent their aggregation. To determine the atomic ratios of Sn, the X-ray absorption spectroscopy (XAS) technique was employed on these samples treated at 650 and 700 °C. The Sn L3-edge curves of these products are shown in Figure 2i and the pure SnO_2 and Sn are selected as the standard ones. As compared to the standard samples' 3L-edge curve, the co-existence of Sn and SnO_2 in the samples can be further proved. Subsequently, the atomic ratios of Sn ($Sn/(Sn+SnO_2)$) could be determined by the fitting process. The results clearly show that the Sn/SnO_2@C samples gained at 700 °C exhibits a larger Sn atomic ratio as compared to the samples prepared at 650 °C. Meanwhile, at identical temperatures, the larger adding amounts of glucose may lead to the decrease in the Sn atomic ratios. The atomic ratios of Sn are 17.5%, 11.1%, 8.1%, 5.9%, 4.8% for samples treating Sn-30, Sn-45, Sn-60, Sn-75, Sn-90 at 650 °C, respectively. At 700 °C, their corresponding atomic ratios were estimated to be 87.1%, 80.1%, 64.5%, 53.9%, 28.4%, respectively. The contents of carbon shell for these products

© 2019 WILEY-VCH Verlag GmbH & Co. KGaA, Weinheim

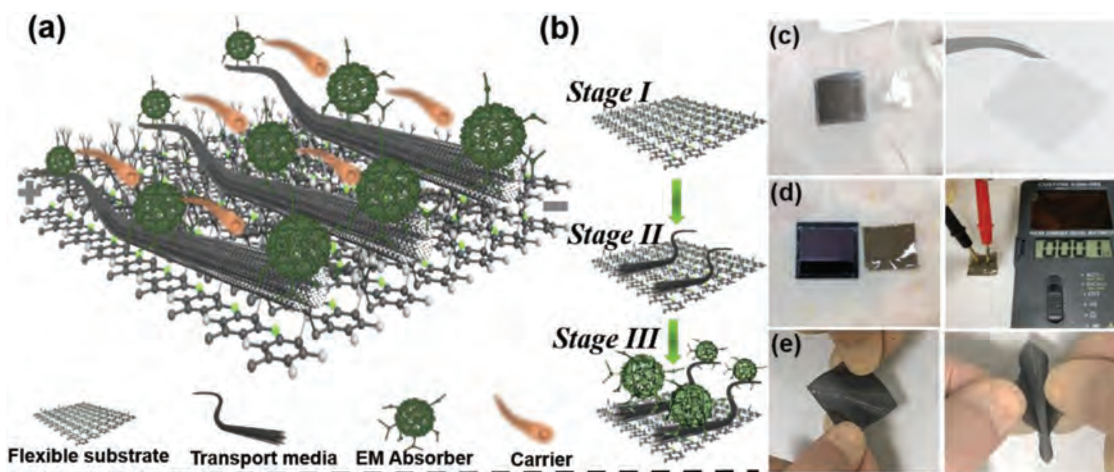

Figure 3. Fabrication of an ET-FA device. a) An ET-FA device constructed by flexible organic polymer layer (parylene-c), carrier transport layer, and EM absorption layer; b) schematic illustration process of the ET-FA device; c–e) the digital photos of the ET-FA device at different stages.

are also tested by thermo gravimetric analyzer (TGA) curves (Figure S4h, Supporting Information) and the actually Sn contents in Sn/SnO_2@C hybrids were summarized in Table S1 (Supporting Information).

To investigate the ET performance, the as-prepared Sn/SnO_2@C products were further employed as an absorption layer to assemble a flexible device (**Figure 3**a). A flexible parylene (type-c, Py-c) film was first grown on a Si/SiO_2 substrate by a chemical vapor deposition (CVD) route (Figure 3b,c, stage I). The correlation between the thickness and the initial amounts of Py-c were measured by surface profile, ensuring the film quality after peeling off from Si/SiO_2 substrate (Figure S5a,b, Supporting Information). Secondly, highly conductive MWCNTs were then overlapped on Py-c by spinning coating to guarantee a good carrier transmission ability (Figure 3b stage II, Figure 3d and Figure S5c–e, Supporting Information). To ensure the even distribution of MWCNTs on the flexible Py-c film, dimethyl sulfoxide (DMSO) as a good organic surfactant was added into the MWCNTs slurry. Before spinning coating, the slurry was treated with powerful ultrasonication for a long time. During spinning coating, a high speed (3000 rpm) for spinning coating is selected. Once spinning coating was finished, the formed film should be baked immediately at 120 °C for 5 min to reduce agglomeration. Lastly, the flexible Py-c/MWCNTs was used as the substrate for overlaying absorber layer (Figure 3e), and the final device is denoted as ET-driven flexible absorber (ET-FA) device. The thickness of Py-c, MWCNTs and absorption layer tested by a KLA Tencor Profiler was estimated to be 5.3, 0.3, and 101.7 µm, respectively (Figure S6, Supporting Information).

Figure 4a plots the permittivity values versus Sn contents for these ET-FA devices. It can be found that a larger Sn content leads to a higher permittivity value. Meanwhile, a larger dielectric value can be obtained for the sample treated with higher temperature. Even so, all measured ε_r values are smaller than lower limit (desirable region: $20 < \varepsilon_r < 60$). Consequently, they only exhibit a good high-frequency absorption performance (ranging from 8.0 to 18.0 GHz). Because of the larger permittivity value, the tunable regions (7.7–13.4 GHz) of ET-FA device treated at 700 °C significantly shift toward lower frequency region, as compared to the devices made by 650 °C (10.4–15.5), and thus it was selected for the subsequently voltage-tuning investigation (Figure 4b and Figure S7a, Supporting Information). Figure 4c and Figure S7b–e (Supporting Information) show the permittivity values of these ET-FA devices (treated at 700 °C) at elevated voltages (0–20 V). Both ε_r–ε'' values undergo activation, enhancement and saturation stages. The critical voltages between enhancement-saturation are denoted as V_s. Commonly, a larger ΔV (V_s–V_a) value contributes to the tuning-amplitude of permittivity. The V_a and V_s values of devices are shown in Figure 4d. For comparison, V_a and V_s values of Sn/SnO_2@C are also given in Figure S7f (Supporting Information). Both V_a and V_s values of ET-FA devices are significantly lower than their respective values, owing to the carrier transmission layer of MWCNTs. Sn-30 device exhibits the smallest V_a and V_s values (3.0 and 14 V), while Sn-90 device possesses the largest V_a and V_s values (10 and 18 V). The variation of V_a may be determined by the carrier mobility, which is associated with component and nanostructure (Figure S7g, Supporting Information).[22–26] The average thickness of carbon shell within Sn-30, Sn-45, Sn-60, Sn-75, and Sn-90 is plotted in Figure 4e. It should be noted that the shells of Sn-75 and Sn-90 products are a half distance between two adjacent cores because one shell is shared by two cores. Among these samples, the shell thickness increases first and then decrease after reaching to a maximum value (≈13 nm). Furthermore, the graphitization level of the graphited area for carrier mobility at both flake or spherical-shaped 3D carbon framework (Figure 4f) can be tuned by changing carbonization temperature or doping elements (e.g., metal, sulfur and nitrogen).[27] In our case, the effect of carbonization temperature on graphitization level can be ignored since all samples were treated at the same temperature. Nevertheless, the high-resolution TEM (HRTEM) image in Figure 4g confirms the existence of Sn-doped nanoparticle in the shell region with a lattice spacing of 0.279 nm (as marked in while color). The Sn dotted carbon shell is due to the diffusion effect under a high temperature.

To further reveal metal diffusion, an in situ XRD characterization was performed by heating Sn@C sample (obtained by

 © 2019 WILEY-VCH Verlag GmbH & Co. KGaA, Weinheim

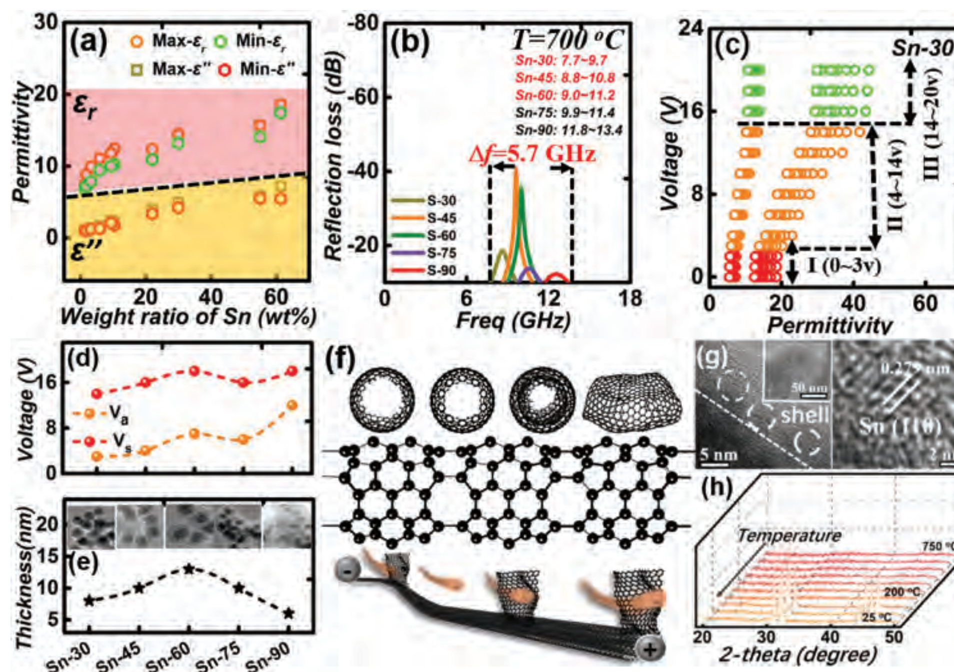

Figure 4. ET-FA devices and voltage-response ability. a) The initial permittivity values of these ET-FA devices as made by these $Sn/SnO_2@C$ products (with different Sn contents, treated $SnO_2@PB$ at 650 or 700 °C); b) the frequency dependence of RL curve for the ET-FA devices (only RL ≤ −10 dB is shown and the absorber is treated by 700 °C); c) the measured permittivity value for the Sn-30 device at a voltage of 0–20 V; d,e) activated (V_a), saturated voltage (V_s), and thickness for these ET-FA devices ($Sn/SnO_2@C$ used here all treated by 700 °C); f) schematic illustration of the 3d carbon network structure and the graphitized area for carrier mobility; g) HRTEM images of a shell region for the product gained at 700 °C (using Sn-60); h) in situ XRD patterns of product heated up to 750 °C and then cooled down to room temperature.

treated Sn-60 at 750 °C) with 750 °C first and then cooled down to room temperature. The temperature dependence of XRD patterns at every 100 °C was provided in Figure 4h. There are no Sn diffraction peaks at temperature regions of 750–300 °C due to the low melting point of Sn (≈273 °C). Until the temperature cooled to 200 °C, Sn diffractions peaks are appeared. In this work, since liquid Sn nanoparticles are obtained at a higher temperature over 600 °C, they diffuse easily into carbon shell. Once more Sn are yielded, the content of inserted Sn in shell increases, as indirectly confirmed by XPS (Figure S7h, Supporting Information). The contribution of Sn dotted carbon to graphitized levels can also be revealed by Raman spectra. It is widely believed that carbon material usually displays two distinguishable peaks in the range of 1000–2000 cm^{-1}.[28–30] One peak is at ≈1350 cm^{-1} (D band) corresponding to the vibrations of sp^3 carbon atoms of disordered graphite. Another peak is at 1590 cm^{-1} (G band) which is ascribed to the in-plane vibration of sp^2 carbon atoms in a 2D hexagonal lattice. Commonly, the graphitization degree of the material can be represented by the intensity ratio of I_D/I_G. As shown in Figure S7i (Supporting Information), the I_D/I_G value gradual increases from 0.84 to 1.04 for these samples obtained at 700 °C, revealing the decrease of graphitization level, even they were treated at the same temperatures. The variation of graphitization level may be due to the differently dotted contents of Sn. After removing Sn (by treating these samples with HCl), the ratio exhibits a slight enhancement as compared to sample without treatment, indicating the decreased graphitization level (Figure S7i, Supporting Information). Hence, it can be deduced that inserted Sn is benefit to a lower ratio of I_D/I_G, enabling to provide more channels for carrier mobility. Based on the analysis of graphitized degree and shell thickness, the variation tendency of V_a for these devices can be fully understood. Particularly for Sn-90, the sharply enhancement of V_a (up to 10 V) is due to the poor graphitization degree and limited channels. As for the V_s, it is attributed to the maximum synergistic effect of integrated mobility (referring to Sn/SnO_2@carbon) and electrical-excited carriers.

The integrated mobility can be further revealed by the electrochemical impedance spectra (EIS), in which Sn-30 sample has the smallest semicircular (carrier transfer resistance, R_{ct}), indicating the strongest carrier mobility (**Figure 5**a).[31] The smallest semicircular for Sn-30 may be attributed to the largest content of metallic Sn, according to the results of controlling experiments, e.g., tuning shell thickness, Sn contents and graphitization level (Figure S7j,k and the inserted images of Figure 5a, Supporting Information). A stronger integrated mobility would result in a smaller V_s value. In addition to mobility, the maximum excitable carrier density (η) also plays a key role on the V_s values. As for $Sn/SnO_2@C$ composite hybrids, η represents the separation ability between electron and holes, which can be estimated by the bandgap (E_g).[32] According to the UV–vis diffuse reflectance spectra (Figure S7l, Supporting Information), the E_g values of these devices are lower than theoretical value of SnO_2 (E_g = 3.8 eV) (Figure 5b). The lowest E_g of 2.6 eV is obtained for Sn-30 device, while the largest one equals to 3.1 eV (Sn-90). Due to a lower E_g value, more electrons can be excited from valance to conductive band under an identical voltage.

© 2019 WILEY-VCH Verlag GmbH & Co. KGaA, Weinheim

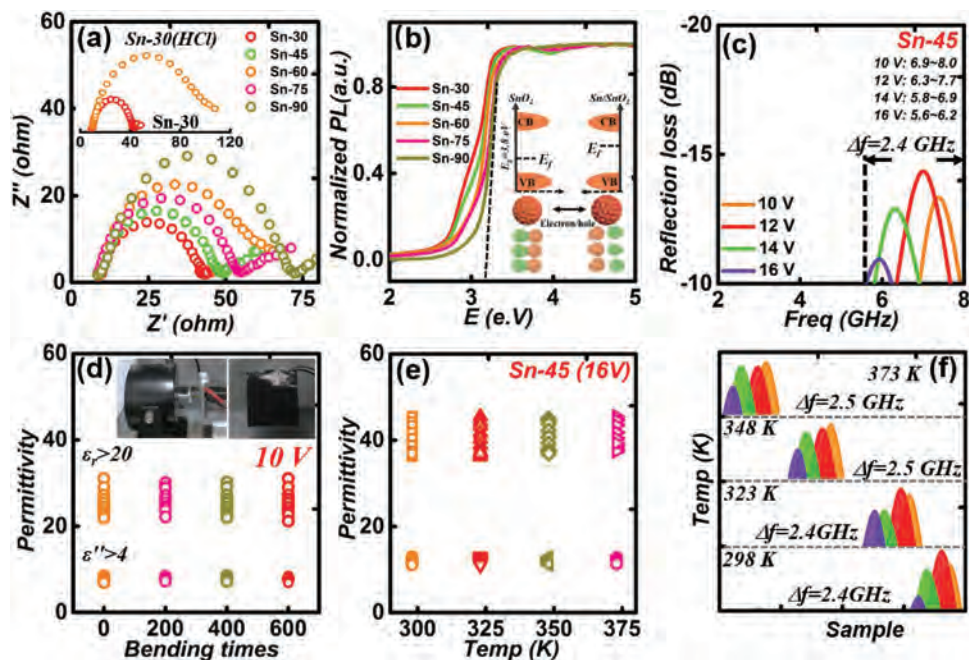

Figure 5. Electrically switchable electromagnetic absorption of ET-FA device. a) EIS spectra of these samples; (inserted image compares samples before and after treated by HCl); b) the converted UV–vis diffuse reflectance curves for these samples (inserted images show the state of VB and CB for SnO_2 and Sn/SnO_2 hybrids); c) the qualified f_E regions for ET-FA device (Sn-45); d) the permittivity values of the optimal ET-FA device (Sn-45) after bending 600 times; e) the temperature-dependent of permittivity of the optimal ET-FA device (Sn-45) with an applied voltage of 10 V; f) the qualified f_E regions of the ET-FA device (Sn-45) as tested at a temperature ranging from 298 to 373 K.

Meanwhile, the excitable electrons are easily saturated at a smaller voltage. At elevated voltage of 0–20 V, the qualified ε_r–ε'' pairs are extracted and applied to draw the RL curves. As shown in Figure 5c and Figure S8a–c (Supporting Information), device with Sn-45 sample exhibits multiple f_E regions ($N = 4$), covering 5.6–8.0 GHz ($\Delta f = 2.4$ GHz). The N of Sn-30 and Sn-60 are estimated to be 3 and 2, respectively (0 for Sn-75 and Sn-90). The optimal Sn-45 device also exhibits an exceptional flexibility after bending 600 times (Figure 5d and Figure S8d–f, Supporting Information). Additionally, the electrical-driven device always generates joule heat after operation for a long time. Thus, the thermal stability is critical for a desirable device. It can be seen in Figure 5f that the dielectric exhibits no significant changes at elevated temperature (up to 373 K, $V = 16$ V), (Figure 5h), implying the almost unchanged EM performance and superior thermal stability.

Although Sn-45 device exhibits a good flexibility and thermal stability, it had a very small ΔV and a relatively large V_a, which influence the qualified numbers of f_E and coverage in C-band. In order to broaden ΔV, an efficient solution is to further finely tune the components, especially for Sn to either reduce V_a or improve V_s. Besides, the initial dielectrics of device need to be close to the lower limit of qualified dielectric pairs. The key to fine-tune the Sn content is to control the starting contents of SnO_2, which is realized here by incorporation of SnS. The as-prepared SnS/SnO_2@C was utilized and then heated at specific temperatures to form $Sn/SnS/SnO_2$@C hybrids. In this regards, the amount of Sn is determined by temperature and the initial SnO_2 content. The synthesis route for $Sn/SnS/SnO_2$@C is illustrated in **Figure 6**a. Specifically, the SnO_2@PB was mixed with a certain amount of thioacetamide (TAA) in a porcelain boat and then heated at 500 °C. During the annealing process, H_2S would be released by TAA and react with SnO_2 to form SnS. Afterward, $Sn/SnS/SnO_2$@C and Sn/SnS@C can be prepared by second annealing at 700 and 750 °C, respectively. Phase structure of samples was investigated by XRD (Figure S9 a–c, Supporting Information). Figure 6b,c shows TEM images of SnS/SnO_2@C sample prepared with 35 mg of TAA (Sn-45 as the precursor). The SnS/SnO@C still maintained a core–shell feature except that the center of the core was a void, as compared to initial SnO_2@C, which may be caused by the sulfidation process. The HADDF-STEM image confirms the uniform distribution of Sn, S, and O elements (Figure 6c). After treated at 700 °C, the core was loose because of the phase conversion from SnO_2 to Sn (Figure 6d). Until to 750 °C, the core consisting of only Sn and SnS turned to be dense, which may be due to the recrystallization at high temperature (Figure 6e and Figure S9d,e, Supporting Information). To get more information about the core, the composites (SnS/SnO_2@C, $Sn/SnS/SnO_2$@C, and Sn/SnS@C) were pre-treated using the Ar-cluster etching technique. The etching parameters and corresponding XPS spectra of Sn 3d are shown in Figure 6f and Table S2 (Supporting Information). As for $Sn/SnS/SnO_2$@C, the peaks of 487.0 and 495.1 eV are ascribed to Sn $3d_{5/2}$ and Sn $3d_{3/2}$ of Sn^{2+} (SnS), respectively, while the peaks of 486.2 and 495.2 eV should be assigned to Sn $3d_{5/2}$ and Sn $3d_{3/2}$ of metallic Sn. The Sn $3d_{5/2}$ and Sn $3d_{3/2}$ of Sn^{4+} (SnO_2) can be observed at 487.9 and 496.4, respectively. As compared to $Sn/SnS/SnO_2$@C, the 3d peaks of Sn element (including Sn^{2+} and Sn) in Sn/SnS@C shift to higher binding energies. But

© 2019 WILEY-VCH Verlag GmbH & Co. KGaA, Weinheim

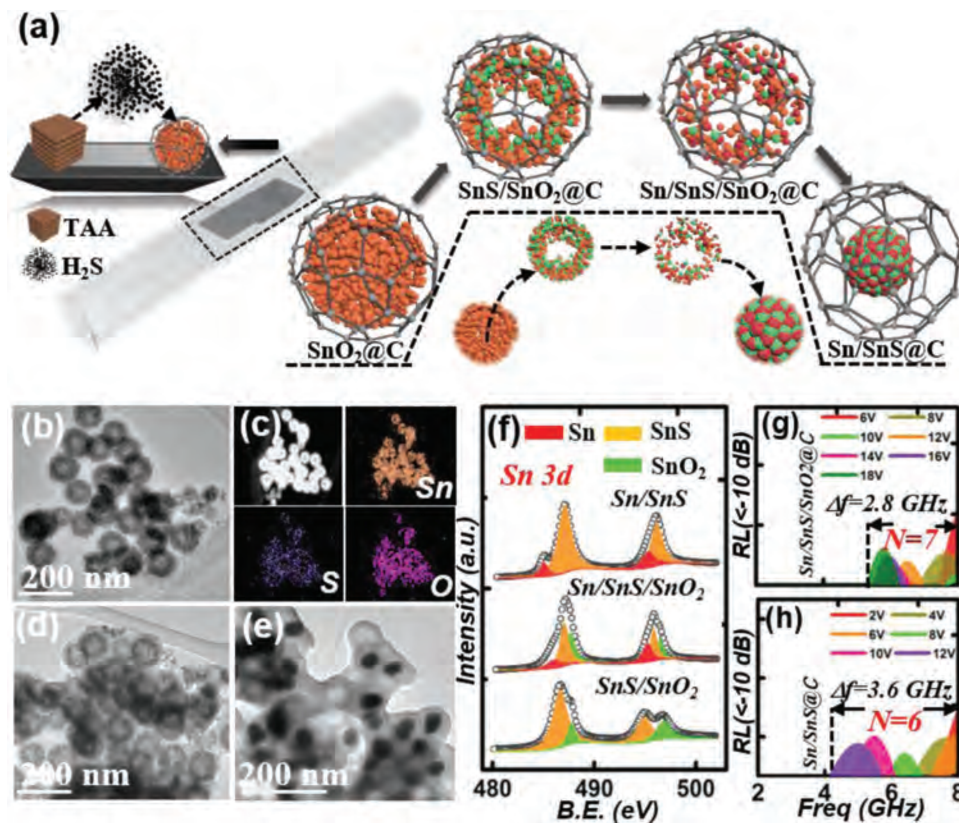

Figure 6. Electrically switchable $Sn/SnS/SnO_2@C$ and Sn/SnS@C-based EM absorption devices. a) The schematic illustration of the formation of $SnS/SnO_2@C$; b) TEM and c) HADDF-STEM images of $SnS/SnO_2@C$; d,e) TEM images of sample obtained by heated $SnS/SnO_2@C$ at 700 and 750 °C, respectively; f) Ar-etched XPS spectra of $SnS/SnO_2@C$, $Sn/SnS/SnO_2@C$, and Sn/SnS@C; g,h) the qualified f_E regions for the optimal $Sn/SnS/SnO_2@C$ and Sn/SnS@C samples.

Sn^{4+} for $SnS/SnO_2@C$ products is turned to be lower binding energy. The phenomenon for blue or red shift is attributed to the mutual coupling effect between components.[33] As a result, the mobility as well as initial permittivity of SnS-containing are larger than the samples without SnS (i.e., $SnS/SnO_2@C>SnO_2@C$, $Sn/SnS@C>Sn/SnO_2@C$) (Figure S9f, Supporting Information). Whereas, a higher mobility would reduce V_a value.

To balance mobility and initial permittivity, a series of $SnS/SnO_2@C$ samples were prepared by reducing the TAA amounts (15 and 25 mg), and then annealed at 700 and 750 °C. The detailed information, e.g., components, contents and voltage dependent of permittivity are summarized in Figure S9g, Figure S10 and Table S3 (Supporting Information). After extracting the qualified permittivity pairs and then calculating RL curves, the largest N can up to 7 for the $Sn/SnS/SnO_2@C$ device (prepared with 25 mg), and corresponding Δf covers 2.8 GHz (Figure 6g, Figure S11 and Figure S12, Supporting Information). While for Sn/SnS@C devices, the maximum N equals to 6 (made by 35 mg), and shows the broadest Δf (3.6 GHz, 90% of coverage) under applied voltages of 2–12 V, as shown in Figure 6h. The excellent tunable performance in C-band is attributed to the initial permittivity, desirable ΔV, and suitable increased amplitude at every given voltage. Meanwhile, both the optimal devices show poor electromagnetic absorption performance in other bands, e.g., L, Ku, and X band, confirming their excellent selective absorption ability (Figure S13, Supporting Information).

3. Conclusions

In summary, we have innovatively developed an electrical switch-driven flexible electromagnetic absorbing device constructed by insulated a parylene-c substrate, a MWCNTs carrier transmission layer and a core–shell nanocomposite with tunable phase and composition absorber. As an example, a flexible device with $Sn/SnS/SnO_2@C$ composite absorber exhibited an exceptional electrically switchable capability and could achieve a narrow ($f_E < 2.0$ GHz), selective and multiple f_E regions ($N = 7$) in 90% of *C*-band. This work provides a promising strategy in developing flexible and intelligent EM absorbing device with desired lower-frequency selectivity.

Supporting Information

Supporting Information is available from the Wiley Online Library or from the author.

Acknowledgements

H.L. and Z.Y. contributed equally to this work. The authors would like to acknowledge the financial support from the National Natural Science

© 2019 WILEY-VCH Verlag GmbH & Co. KGaA, Weinheim

Foundation of China (Nos. 51672049, 51602054 and 51871060), Recruitment Program of Global Youth Experts, China Postdoctoral Science Foundation (No. KLH2921060), and FDUROP (Fudan's Undergraduate Research Opportunities Program).

Conflict of Interest

The authors declare no conflict of interest.

Keywords

fine-tune components, flexible electric-driven devices, linear-regulation of permittivity, selective EM absorption, switchable

Received: September 2, 2019
Revised: October 4, 2019
Published online:

[1] F. Shazad, M. Alhabeb, C. B. Hatter, B. Anasori, S. M. Hong, C. M. Koo, Y. Gogotsi, *Science* **2016**, *353*, 1137.
[2] S. K. Lee, I. Jo, S. Kang, B. Jang, J. Moon, J. B. Park, S. Lee, S. C. Rho, Y. Kim, B. H. Hong, *ACS Nano* **2017**, *11*, 5318.
[3] Z. H. Yang, H. L. Lv, R. B. Wu, *Nano Res.* **2016**, *9*, 3671.
[4] H. L. Lv, Y. H. Guo, Z. H. Yang, T. C. Guo, H. J. Wu, G. Liu, L. Y. Wang, R. B. Wu, *ACS Sustainable Chem. Eng.* **2018**, *6*, 1539.
[5] F. Ye, Q. Song, Z. C. Zhang, W. Li, S. Y. Zhang, X. W. Yin, Y. Z. Zhou, H. W. Tao, Y. S. Liu, L. F. Cheng, L. T. Zhang, H. J. Li, *Adv. Funct. Mater.* **2018**, *28*, 1707205.
[6] Z. C. Wu, K. Pei, L. S. Xing, X. F. Yu, W. B. You, R. C. Che, *Adv. Funct. Mater.* **2019**, *29*, 1901448.
[7] Q. Li, Z. Zhang, L. P. Qi, Q. L. Liao, Z. Kang, Y. Zhang, *Adv. Sci.* **2019**, *8*, 1801057.
[8] X. L. Li, X. W. Yin, C. Q. Song, M. K. Han, H. L. Xu, W. Y. Duan, L. F. Cheng, L. T. Zhang, *Adv. Funct. Mater.* **2018**, *28*, 1803938.
[9] H. Lv, Y. H. Guo, Z. H. Yang, Y. Cheng, L. Y. P. Wang, B. S. Zhang, Y. Zhao, Z. C. J. Xu, G. B. Ji, *J. Mater. Chem. C* **2017**, *5*, 491.
[10] H. Abbasi, M. Antunes, J. I. Velasco, *Prog. Mater. Sci.* **2019**, *103*, 319.
[11] Y. L. Zhang, X. X. Wang, M. S. Cao, *Nano Res.* **2018**, *11*, 1426.
[12] F. Cao, L. X. Meng, M. Wang, W. Tian, L. Li, *Adv. Mater.* **2019**, *31*, 1806725.
[13] S. Wang, J. Xu, W. C. Wang, G. J. N. Wang, R. Rastak, F. Lopez, J. W. Chung, S. M. Niu, V. R. Feig, J. Lopez, T. Lei, Y. Kim, A. M. Foudeh, A. Ehrlich, A. Gasperini, Y. J. Yun, B. Murmann, J. B. H. Tok, Z. N. Bao, *Nature* **2018**, *555*, 83.
[14] S. Baik, H. J. Lee, D. W. Kim, J. W. Kim, Y. Lee, C. Y. Pang, *Adv. Mater.* **2019**, *31*, 1803309.
[15] L. S. Xie, L. Sun, R. M. Wan, S. S. Park, J. A. Degayner, C. H. Hendon, M. Dinca, *J. Am. Chem. Soc.* **2018**, *140*, 7411.
[16] V. Fatemi, S. F. Wu, Y. Cao, L. Bretheau, Q. D. Gibson, K. Watanabe, T. Taniguchi, R. J. Cava, P. J. Herrero, *Science* **2018**, *362*, 926.
[17] Y. Li, X. F. Liu, X. Y. Nie, W. W. Yang, Y. D. Wang, R. H. Yu, J. L. Shui, *Adv. Funct. Mater.* **2019**, *29*, 1970059.
[18] M. S. Cao, X. X. Wang, W. Q. Cao, X. Y. Fang, B. Wen, J. Yuan, *Small* **2018**, *14*, 1800987.
[19] O. Balci, E. O. Polat, N. Kakenov, C. Kocabas, *Nat. Commun.* **2015**, *6*, 6628.
[20] X. N. Zhao, H. P. Liu, J. Y. Yu, Y. X. Li, Y. H. Zhang, X. F. Zhang, *IEEE Trans. Magn.* **2018**, *9*, 2800705.
[21] X. F. Zhou, Z. R. Jia, A. L. Feng, X. X. Wang, J. J. Liu, M. Zhang, H. J. Cao, G. L. Wu, *Carbon* **2019**, *152*, 827.
[22] G. Soavi, G. Wang, H. Rostami, D. G. Purdie, D. D. Fazio, T. Ma, B. Luo, J. J. Wang, A. K. Ott, D. Yoon, S. A. Bourelle, J. E. Muench, I. Goykhman, S. D. Conte, M. Celebrano, A. Tomadin, M. Polini, G. Cerullo, A. Ferrari, *Nat. Nanotechnol.* **2018**, *13*, 583.
[23] M. A. Caro, V. L. Deringer, J. Koskinen, T. Laurila, G. Csanyi, *Phys. Rev. Lett.* **2018**, *120*, 166101.
[24] T. Wei, O. Martin, S. F. Yang, F. Hauke, A. Hirsch, *Angew. Chem., Int. Ed.* **2019**, *58*, 816.
[25] H. Patel, L. J. Huang, C. J. Kim, J. Park, M. W. Graham, *Nat. Commun.* **2019**, *10*, 1445.
[26] M. S. Cao, X. X. Wang, M. Zhang, J. C. Shu, W. Q. Cao, H. J. Yang, X. Y. Fang, J. Yuan, *Adv. Funct. Mater.* **2019**, *29*, 1807398.
[27] S. S. Liu, M. F. Wang, X. Y. Sun, N. Xu, J. Liu, Y. Z. Wang, T. Qian, C. L. Yan, *Adv. Mater.* **2018**, *30*, 1704898.
[28] Z. L. Chen, R. B. Wu, M. Liu, H. Wang, H. B. Xu, Y. H. Guo, Y. Song, F. Fang, D. L. Sun, *Adv. Funct. Mater.* **2017**, *27*, 1702046.
[29] Z. L. Chen, R. B. Wu, Y. Liu, Y. Ha, Y. H. Guo, D. L. Sun, M. Liu, F. Fang, *Adv. Mater.* **2018**, *30*, 1802011.
[30] Y. Liu, Z. L. Chen, H. X. Jia, H. B. Xu, M. Liu, R. B. Wu, *ACS Nano* **2019**, *13*, 6113.
[31] L. Tao, M. Qiao, R. Jin, Z. H. Xiao, Y. Q. Wang, N. Zhang, C. Xie, Q. G. He, D. C. Jiang, G. Yu, Y. F. Li, S. Y. Wang, *Angew. Chem., Int. Ed.* **2018**, *58*, 1019.
[32] F. Ambrosio, J. Wiktor, F. D. Angelis, A. Pasquarello, *Energy Environ. Sci.* **2018**, *11*, 101.
[33] Y. Zhang, T. F. Zhou, C. F. Zhang, J. F. Mao, H. K. Liu, Z. P. Guo, *Angew. Chem., Int. Ed.* **2016**, *55*, 3408.

© 2019 WILEY-VCH Verlag GmbH & Co. KGaA, Weinheim